Analysis of Polymeric Methylaluminoxane (MAO) via Small Angle Neutron Scattering

Jörg Stellbrink,*,† Aizhen Niu,† Jürgen Allgaier,† Dieter Richter,† Bernd W. Koenig,‡ Rudolf Hartmann,‡ Geoffrey W. Coates,§ and Lewis J. Fetters||

Institut für Festkörperforschung, Forschungszentrum, Jülich GmbH, 52425 Jülich, Germany, Institut für Biologische Informationsverarbeitung 2, Forschungszentrum, Jülich GmbH, 52425 Jülich, Germany, Department of Chemistry and Chemical Biology, Cornell University, Ithaca, New York 14853-1301, and School of Chemical and Biomolecular Engineering, Cornell University, Ithaca, New York 14853-5021

Received December 22, 2006; Revised Manuscript Received April 12, 2007

ABSTRACT: Since its discovery as a crucial cocatalyst in metallocene and post-metallocene olefin polymerizations methylaluminoxane (MAO) has retained commercial and academic status. In spite of continued interest the MAO structure remains ambiguously defined. Because of limited alkane solubility toluene emerged as the MAO solvent of necessity. With time these toluene solutions can develop a gel fraction. The MAO structures proposed include linear, ring, ladder, and cyclic with the latter involving fused four and six membered rings along with cage and drumlike architectures. The linear and ring structures have aluminum and oxygen valences of three and two respectively while the other structures require Al/O co-ordination numbers of four and three. MAO structural information has been gathered from colligative property measurements, various NMR formats and quantum chemical calculations. We have used small-angle neutron scattering (SANS)—fortified with static and dynamic light scattering (SLS/DLS)—as the primary analysis tool for dilute MAO solutions ($\phi/\phi^* \leq 0.6$). The main structure assayed is a linear polymer chain consisting of [−Al(CH_3)−O−] monomer units with an M_w of 20 kg/mol and a negative second virial coefficient. The latter fortifies the recognized state of play that toluene is a poor MAO solvent. About 0.8 wt % of MAO was captured as large-scale three-dimensional aggregates. Elemental analysis results show that in these large-scale aggregates the ratio of O/Al is significantly larger than for the smaller polymer chains. Additionally the large-scale aggregates contain only a small fraction of CH_3 units. Those structures may be the precursor aggregates to the previously observed macroscopic gel fraction reported to form over time at room temperature. The solutions studied in this work did not show gel formation over an 8-month period at ∼0 °C.

Introduction

Methylaluminoxane ([Al/CH_3/O]−MAO) has held, since its discovery as a catalyst activator in 1980,[1,2] a nearly unique position as the activating cocatalyst for olefin-based polymerizations. The absolute structural identities of the MAO aggregates and its catalyst complexed counterparts remain ill-defined. The need for sufficient propagating headgroup reactivity often requires a MAO/catalyst ratio $>10^4$. Supported catalyst systems can reduce this value. This generic dual catalyst combination led to the commercialization of olefin homo- and copolymerizations presumably carried by a single active center, the "single site" systems.[3] The monolithic identity of the propagating site has led to unprecedented compositional, molecular weight distribution and tacticity control in olefin systems. In certain cases, the propagation mechanism yields living systems[4] that provide control over chain molecular weights and polydispersity indices.

MAO is taken to be a Lewis acid that substitutes one or both chlorides on the catalyst precursor with methyl groups, then abstracts a chloride or methyl group to form the propagating center. These active sites most commonly involve the cation alkyl complexes with Ti, Zr, Hf, or Ni. The Lewis acid character is in agreement with that of tricoordinated aluminum found in the self-assembled linear or ring architectures. Sinn et al.[5] have referred to this form of [−Al(CH_3)O−] as "classic" MAO. Quantum chemical calculations[6] (based upon the density functional theory) favor triple layer cage structures relative to the linear or ring architectures. The former aggregates involve the coordination numbers of three and four for oxygen and aluminum respectively. The Lewis acid character of aluminum with the dative bond is attenuated relative to that of the trivalent format. Thus, a structure/activity conflict is in play where the trivalent form of aluminum is deemed as having the needed Lewis acid behavior while the favored MAO structures require aluminum to adopt the quadra-valent format with its attendant diminished Lewis acid character.

In contrast to MAO's status as a vital co-ingredient in these systems its molecular structure in solution remains ill-deciphered. For some commercial forms of MAO the chemical compositions[7] are experimentally approximated as follows: [Al/$(CH_3)_{\sim 1.5}$/$O_{\sim 0.75}$]$_n$ where n is an integer taken to range from about 8 to 18. Sinn[8] has dubbed this structure "true" MAO. Cage and drumlike structures[9] have been proposed to represent the MAO architecture. The deviation from the stoichiometric structure ("classic" MAO) of [−Al(CH_3)O−] appears to be dependent upon the MAO synthetic route chosen.[10] Cryoscopy was used to evaluate the molecular weight of MAO aggregates with the finding of values ranging from 700−1200 g/mol.[5,8]

Two formats of NMR have been used to evaluate the MAO molecular size. The proton spin lattice relaxation time technique can, in principle, yield information concerning molecular motion,

* To whom correspondence should be addressed. E-mail: j.stellbrink@fz-juelich.de.
† Institut für Festkörperforschung, Forschungszentrum, Jülich GmbH.
‡ Institut für Biologische Informationsverarbeitung 2, Forschungszentrum, Jülich GmbH.
§ Department of Chemistry and Chemical Biology, Cornell University.
|| School of Chemical and Biomolecular Engineering, Cornell University.

10.1021/ma062940v CCC: $37.00
Published on Web 06/12/2007

viscosity and dimensions of the diffusing molecule.[11] This approach has led to an effective radius of 12.2−14.4 Å for a MAO anion tethered to a Zr-based cation.

Pulsed field gradient NMR indicates the value of 19.4 Å as the molecular size of the MAO molecule.[12] Reviews are available that survey proposed MAO structures.[10,13,14] A survey of this literature reveals that cyclic and long chain linear structures with their tricoordinate aluminum character seemingly have been dismissed as viable aggregate architectures. An accepted rationale for this is the conclusion[15] that "such coordination is rare in aluminum chemistry and can be found only when higher coordination is sterically hindered". The MAO structure literature is generally mute, in a quantitative manor, as to why large-scale aggregates involving trivalent aluminum are unfeasible.

We have examined the structure of MAO in d_8-toluene using small-angle neutron scattering (SANS) complimented with static and dynamic light scattering (SLS and DLS). In general we found three different regimes in the scattering behavior of all MAO solutions. (i) At small scattering vectors, $Q \leq \sim 6 \times 10^{-3}$ Å^{-1} as covered by SLS and partly by SANS, we observed a strong power law decay of the scattering intensity, $I(Q) \sim Q^{-4}$, typical for sharp interfaces between dispersed particles and solvent[16] (asymptotic regime, Porod scattering). (ii) At intermediate Q vectors, 6×10^{-3} Å$^{-1} \leq Q \leq 0.03$ Å^{-1} as covered by SANS only, we observed a concentration dependent intensity plateau. Finally (iii) at large Q vectors, $Q \geq 0.1$ Å^{-1}, a second asymptotic regime is found with a power law decay of the scattering intensity, $I(Q) \sim Q^{-2}$, typical for a Gaussian polymer coil.[17] This scenario can be interpreted by the presence of two different species of scattering particles with strongly different radii of gyration. The larger particles are too big for their size to be precisely determined. Only their asymptotic regime i is seen in our scattering experiments. For the smaller particles, on the other hand, we can precisely determine their radius of gyration, $R_g = 46.2$ Å, and molecular weight, $M_w = 20$ kg/mol, from regime ii. The asymptotic regime iii of the smaller particles shows that their internal structure resembles those of linear polymer chains (Gaussian coils).

With respect to the corresponding weight fractions of the two species, we found that the linear polymer chain (Gaussian coil) was observed to be the main structure in dilute solution. With increasing concentration we found branching to occur via interchain coordination. Only a very small fraction (≤0.8%) of MAO is present as large scale particles. No evidence of the coexistence of the smaller structures conjectured by others[10,13−15] was found.

Experimental Section

A. MAO Purification and Isolation. Polymethylaluminoxane−IP (PMAO−IP) was obtained from Akzo-Nobel as a transparent, colorless and precipitant free toluene solution.[18] The aluminum content was 7 wt %. Sample preparation was carried out on a vacuum line and in an MBraun Unilab glovebox under argon atmosphere (O_2 level < 0.1 ppm, H_2O level < 1 ppm). All equipment that was used outside the glovebox was equipped with Teflon Young stopcocks to prevent contamination with air or moisture. These procedures emulate the protocols previously given[19] for the rigorous handling and purification of the solvents and monomers used in organolithium living anionic polymerizations. Hence, the possibility of accidental sample adulteration was virtually eliminated.

Using the glovebox, the PMAO−IP solution was transferred into a flask. The toluene was then distilled off at 50 °C on the vacuum line. To ensure removal of residual trimethyl aluminum (TMA) the pumping process was continued overnight at the same temperature. A white solid remained. The weight corresponded to 17.7% of the original solution. Deuterated toluene (99% d, Chemotrade) was purified by three degassing cycles, stirred for several days (on the vacuum line) over sodium dispersion at room temperature followed by 3 h stirring at 110 °C. Finally the d_8-toluene was distilled into a second flask.

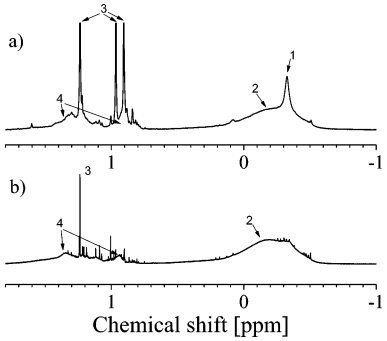

Figure 1. ^{1}H NMR spectra of PMAO−IP in d_8-toluene at 20 °C. (a) Original PMAO−IP. (b) After removal of TMA.

Samples for ^{1}H NMR, SLS/DLS, and SANS were obtained by dissolving solid PMAO−IP in d_8-toluene. Before use the d_8-toluene was filtered (in the glovebox) using a 0.02 μm Anotop membrane filter (Whatman, U.K.). Static light scattering demonstrated that the d_8-toluene was dust free. All cells, flasks, and pipettes used for this work were likewise prepared dust free by extensively rinsing with filtered acetone in the glovebox. The cells containing the solutions were prepared in the glovebox and transferred to the vacuum line, cooled to ∼−80 °C, evacuated, and flame-sealed off. For some samples the PMAO−IP solutions were centrifuged for different times using a Heraeus Labofuge 400R at 4500 rpm before being transferred into the cells.

For the sample that was centrifuged for 1 h the amount of precipitate was quantified. After centrifugation the clear solution was removed almost quantitatively in the glovebox, new dry toluene was added to wash the precipitate and the centrifugation process was repeated for another 2.5 h. Again the clear solution was removed and the flask containing the precipitate was dried under high vacuum conditions. It was found that the precipitate accounted for 0.8 wt % of the solid PMAO−IP originally used for the experiment.

Historically MAO has been produced via the reaction of water with trimethyl aluminum (TMA). Toluene solutions of this material lack long-term stability since gels and solid material can form as a function of time. The PMAO−IP studied in this work was produced by a nonhydrolytic process.[18] Generally, the way MAO is produced has strong influence on its chemical composition.[14] As will be shown, this synthetic approach yields a product with a composition approaching that of "classic" polymeric MAO [−Al(CH_3)O−].

B. ^{1}H NMR of PMAO—IP. The purity of PMAO−IP in d_8-toluene was evaluated by proton NMR. One-dimensional NMR spectra were recorded on a 14.1 T instrument (Varian Unity Inova 600) at 20 °C. Eight scans were accumulated for each spectrum using a long recycling delay (30 s) between scans. The integral peak intensity is proportional to the number of protons contributing to a signal only if the spin system completely relaxes between consecutive scans.

The primary impurity was considered to be TMA. NMR spectra of PMAO−IP in d_8-toluene were recorded prior to and after the purification procedure described above. The spectrum of nonpurified PMAO−IP, Figure 1a, was obtained after diluting 0.1 mL of the original PMAO−IP solution in h_8-toluene with 1 mL of dry d_8-toluene. The broad signal 2 extending from about +0.3 ppm to −0.5 ppm corresponds to methyl protons of PMAO−IP. The narrower peak 1 at −0.3 ppm on top of the broad signal is related to TMA.[1,2] The molar ratio between (Al(CH_3)−O) and TMA is approximately 95:5 based on the integral signal intensities. NMR signals observed between +1.5 ppm and +0.8 ppm (3 and 4) most

Table 1. Characterization of Methylaluminoxane

sample	composition	density [g/cm^3]	ρ [cm^{-2}]
h-MAO(nominal)	$-(AlOCH_3)-$	≈1.036	5.03×10^9
h-PMAO−IP (analysis)	$-(AlOC_{1.45}H_{3.89})-$	≈1.10	4.45×10^9
amorph. aluminum oxide	Al_2O_3	2.85	4.09×10^{10}
decomposed MAO	$Al_2O_{2.5}CH_3$	≈1.90	1.77×10^{10}
h_8-toluene	C_7H_8	0.865−0.867	9.38×10^9
d_8-toluene	C_7D_8	0.943	5.62×10^{10}

likely arise from aliphatic cosolvents or higher alkyl groups that are incorporated into the PMAO−IP structure.[18]

A ^{1}H NMR spectrum of PMAO−IP in d_8-toluene after removal of volatile material is shown in Figure 1b. The almost complete disappearance of the sharp signal at −0.3 ppm indicates that most of the TMA was eliminated. The remaining signals (3 and 4) between +1.5 and +0.8 ppm most likely represent higher alkyl groups, which are covalently bound to PMAO−IP. Octyl groups are frequently incorporated into PMAO−IP for solubility enhancement.[18] We assume that the PMAO−IP studied here also contains octyl groups causing the NMR signals observed between +1.5 and +0.8 ppm. From the intensity ratio of the methyl and octyl peaks in Figure 1b it was estimated that the molar ratio of octyl to methyl is approximately 6:94 in the PMAO−IP studied.

C. Elemental Analysis of PMAO—IP. The elemental analysis of the purified PMAO−IP was carried out in the Zentralabteilung für Chemische Analyze, Forschungszentrum Jülich. For the purified PMAO−IP after removal of TMA the amount of aluminum was found to be 36.9 ± 0.7 wt %, while for oxygen 20.8 ± 1.0 wt % were measured. This translates into an O/Al molar, which is close to the ideal value for "classic" MAO of 1:1. The elemental analysis was also carried out on the precipitate obtained after the centrifugation process. The amount of aluminum was 46.4 ± 0.5 wt % while that of oxygen was 35.3 ± 0.5 wt %. This led to the molar ratio O/Al of 1.28:1.

D. Density Determination of PMAO—IP. The density of neat PMAO−IP was estimated from the densities of the corresponding solutions in h_8-toluene using $d_{PMAO-IP} = (d_{sol.} - (1 - x_{w,PMAO-IP}) \cdot d_{tol.})/x_{w,PMAO-IP}$. For unpurified PMAO−IP solution used in this study the density has a value of 0.90 g/cm^3 at a weight fraction (solid material) of $x_w = 0.177$, which had to be corrected for the amount (5 mol %) of TMA. We thus derived a MAO density of 1.10 g/cm^3; see Table 1. For comparison: compilation of data from different suppliers gave a mean value of $d_{MAO} = 1.04 \pm 0.07$ g/cm^3. (Aldrich, $x_{w,MAO} = 0.1$, $d_{sol.} = 0.875$ g/cm^3; Albemarle, $x_{w,MAO} = 0.1$, $d_{sol.} = 0.89$g/cm^3; Albemarle, $x_{w,MAO} = 0.3$, $d_{sol.} = 0.92$g/cm^3).

Combining all results from ^{1}H NMR and elemental analysis about the chemical composition of PMAO−IP, we can thus assign the following sum formula for purified PMAO−IP: $AlOC_{1.45}H_{3.89}$ and calculate the mean molecular weight of the PMAO−IP monomer unit where CH_3 is partially replaced by the *n*-octyl unit: $M_{MAO} =$ 64.3g/mol.

E. SANS Experiments. The SANS measurement uses wavelengths (λ) from ca. 5 to 15 Å over the angular range of ∼0.1−20°. Therefore, it probes structural dimensions covering the range between 15 Å and several thousand angstroms. Since in the smallest of these spatially resolvable volumes there are many atoms, the system can be described in terms of scattering length densities (ρ_i). The advantage of neutrons over X-rays is the ability to vary the scattering length densities of different constituents of a hydrocarbon sample over a broad range by H/D substitution. The visibility of the molecules in solution depends upon the difference between the solvent/solute scattering length densities.

The experimental quantity observed in a SANS experiment is the intensity in terms of the macroscopic cross section ($d\Sigma/d\Omega$) as a function of the scattering vector $Q = [4\pi/\lambda] \sin \Theta/2$, with λ the neutron wavelength and Θ the scattering angle. Q has the dimensions of a reciprocal length and can therefore be regarded as an "inverse meter stick".

$$\frac{d\Sigma}{d\Omega}(Q) = \frac{\Delta\rho^2}{N_a} \phi V_w P(Q) \quad (1)$$

Here, ϕ is the volume fraction, V_w the corresponding weight-average molecular volume, and $P(Q)$ the form factor of the scattering particles, which contains all structural information. $\Delta\rho$ is the scattering contrast given by

$$\Delta\rho = \rho_0 - \rho = \left[\frac{\sum b_0}{v_0} - \frac{\sum b_{mon}}{v_{mon}}\right] \quad (2)$$

The ratio $\rho_0 = \Sigma b_0/v_0$ is the scattering length density of the solvent with b_0 the scattering length of the atoms forming the solvent molecule and v_0 the corresponding volume. $\rho = \Sigma b_{mon}/v_{mon}$ is the corresponding quantity for the repeat unit of the scattering particle and N_a the Avogadro number. Since all b_i terms are well-defined and tabulated properties of the corresponding nucleus the SANS data are obtained on an absolute scale and can be unambiguously interpreted.

The SANS measurements were performed at the instruments KWS1 and KWS2 at the Forschungszentrum Jülich. We used sample-to-detector distances, $D = 20$, 8, 4, 2, and 1.25 m, and collimation lengths, $L = 20$, 14, 8, 4, and 2 m, using a neutron wavelength $\lambda = 7.3$ Å with a wavelength spread of $\Delta\lambda/\lambda = 20\%$ and 10%, respectively. This covers a Q range of 2×10^{-3} Å$^{-1} \le Q \le 0.23$ Å^{-1}, which corresponds to a spatial resolution 5 Å $\le D = 1/Q \le 500$ Å. To achieve maximum contrast and minimum incoherent background, we investigated the PMAO−IP structure in d_8-toluene. Using eq 2, we can calculate the coherent scattering length density for MAO: $\rho_{MAO} = 4.45 \times 10^9$ cm^{-2} and an incoherent scattering intensity of $(d\Sigma/d\Omega)_{inc.}$ and $\rho_{d-toluene} = 5.62 \times 10^{10}$ cm^{-2} (99% D).

In general, all azimuthally averaged data were corrected for empty cell scattering and then normalized to the absolute scattering cross section, [cm^{-1}], using a 1.5 mm plexi standard. Contributions due to incoherent background and solvent scattering were subtracted from all data sets before analysis. Table 2 lists the contrast matching toluene mixtures used in this work. A useful presentation of the theory and practice of SANS for polymeric systems is available from Higgins and Benoit.[20]

F. Static and Dynamic Light Scattering (SLS/DLS). In order to obtain a maximum degree of comparability between all experiments, the measurements used solutions that were prepared by dilution of the stock solution used for the SANS experiments. Samples were prepared, covering a concentration regime between 1% and 10%. The solutions were filtered through 0.2 μm Anotop membrane filters (Whatman, U.K.) into the thoroughly cleaned sample cells (Hellma). The refractive index, $n_d = 1.49$, and density of the solvent d_8-toluene, $d = 0.943$ g/cm^3 were taken from the literature.[21] The absolute viscosity was estimated to be $\eta_0 = 0.62$ cp (For $T = 273$ K a value of $\eta_0 = 0.81$ cp is reported for d_8-toluene compared to $\eta_0 = 0.77$cp for h_8-toluene and assuming a T-independent ratio).

DLS experiments were performed using an ALV SP-125 (ALV, Langen, Germany) compact goniometer in a homodyne setup with an argon ion laser (Coherent, Innova 90-4), operating with vertically polarized light at 514.5 nm, 50−800 mW TEM. Intensity autocorrelation functions $g^2(Q,t)$ were recorded with an ALV 5000 E (fast version, 319 channels) multi-τ digital correlator covering a time window from 12.5 ns up to several hours. The scattering vector Q for light scattering is given by $Q = [4\pi n_d/\lambda_0]\sin \Theta/2$ with λ_0 the wavelength in vacuum. Because of the use of a dual detector system (ALV−SO/SIPD) operating in the "pseudo" cross-correlation mode even the first channels could be recorded without any distortion from electronic noise. All measurements were performed at 20.0 ± 0.1 °C in the angular range $28 \le \Theta \le 154°$, yielding a Q range from 7.84×10^{-4} to 3.56×10^{-3} Å^{-1}. This compliments the SANS Q range of $2 \times 10^{-3} \le Q \le 0.23$ Å^{-1}.

The measured intensity autocorrelation function $g^2(Q,t)$ can be related to the intermediate scattering functions $g^1(Q,t)$ by the well-

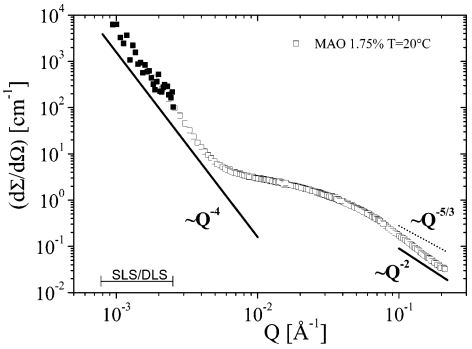

Figure 2. SANS intensity in absolute units vs scattering vector Q. Solid lines: power law with slope −4 (Porod law), −2 (Gaussian chain), and $-(5/3)$ (swollen chain), respectively. Filled symbols: SLS data scaled by a factor $f = 6 \times 10^7$.

Table 2. Solvent Compositions Used for SANS Contrast Variation

solvent composition	ϕ *d*-toluene	density [g/cm^3][a]	ρ [cm^{-2}]
d_8-toluene	1.000	0.943	5.622×10^{10}
63%	0.634	0.914	3.94×10^{10}
41%	0.410	0.897	2.87×10^{10}
18%	0.179	0.879	1.78×10^{10}
h_8-toluene	0.000	0.865−0.867	9.38×10^9

[a] 293 K.

known Siegert relation[22] $g^1(Q,t) = \sqrt{g^2(Q,t)-1}$. Data were analyzed independently by (i) the cumulant method,[23] which expands $\ln(g^1(Q,t))$ in a power series of t: $\ln(g^1(Q,t)) = \mu_0 - \mu_1 t + (1/2!)\,\mu_2\, t^2 - \ldots$, with a first cumulant $\mu_1 = \Gamma$, the mean relaxation frequency, and a reduced second cumulant μ_2/μ_1^2 related to the polydispersity of the sample, and (ii) the inverse Laplace transformation using the regularization algorithm of the CONTIN program.[24] To account for particle interactions in dilute solution, a virial expansion can be made that describes the concentration dependence of the mutual diffusion coefficient $D_m(\phi)$. After extrapolation to infinite dilution, $\lim_{\phi\to 0} D_m(\phi) = \lim_{\phi\to 0} \Gamma_1(\phi)/Q^2 = D_0$ the hydrodynamic radius of the scattering particles can be derived from the Stokes−Einstein relation: $R_h = [kT/6\pi\eta_0 D_0]$.

Results and Discussion

SANS/SLS. Figure 2 shows the SANS scattering intensity $(d\Sigma/d\Omega)$ in absolute units [cm^{-1}] as a function of scattering vector Q for purified PMAO−IP in d_8-toluene at 20 °C with a volume fraction $\phi = 1.75\%$. Also shown are static light scattering (SLS) data (filled symbols, scaled by a factor $f = 6 \times 10^7$) that extend the SANS Q range to smaller scattering vectors. We were not able to experimentally determine the refractive index increment (dn/dc) needed for SLS since all MAO solutions are highly sensitive to air and can only be handled in an inert atmosphere (glovebox). Both data sets, the Rayleigh ratio R_Θ obtained by SLS and the macroscopic scattering cross section $(d\Sigma/d\Omega)$ obtained by SANS, were obtained in absolute units [cm^{-1}] by normalization to either a toluene or a plexi standard, respectively. In general, the molecular volume V_w in cm^3/mol of a scattering particle can only be derived from the experimental scattering intensity in [cm^{-1}], if the contrast factor k of the applied scattering technique is known:

$$\left(\frac{d\Sigma}{d\Omega}\right)(Q,\phi) = \phi k_{SANS} V_w P(Q); \qquad R_\Theta(Q,\phi) = \phi k_{SLS} V_w P(Q) \quad (3)$$

and after extrapolation to zero scattering vector and infinite dilution:

$$\lim_{Q\to 0,\phi\to 0} (d\Sigma/d\Omega) = \phi k_{SANS} V_w, \quad \lim_{Q\to 0,\phi\to 0} R_\Theta = \phi k_{SLS} V_w \quad (4)$$

The corresponding contrast factors for SANS and SLS are given by $k_{SANS} = \Delta\rho^2/N_A$ and $k_{SLS} = (4\pi^2 n_0^2 (dn/dc)^2)/(dN_A\lambda^4)$. From our SLS data alone, it was not possible to derive V_w due to the missing (dn/dc) value. Therefore, we scaled in Figure 2 the normalized SLS data, R_Θ, to the normalized SANS data, $(d\Sigma/d\Omega)$, to show the scattering profile of MAO over the whole experimental Q range. The applied multiplicative factor for the SLS data shown in Figure 2 is $f = 6 \times 10^7$. Hence, in principle we should be able to recalculate the experimentally inaccessible (dn/dc) value for MAO from the applied scaling factor f by starting from

$$\left(\frac{d\Sigma}{d\Omega}\right)_{SANS} = k_{SANS}\phi_{SANS} V_w P(Q) = f R_\Theta^{SLS} = f k_{SLS}\phi_{SLS} V_w P(Q) \quad (5)$$

This then gives

$$\left(\frac{dn}{dc}\right) = \sqrt{\frac{d\lambda^4}{2\pi^2 n_0^2}\frac{\Delta\rho^2}{f}} \quad (6)$$

Using our experimental parameters, n_0=1.494, $\lambda = 514.5$ nm, $\Delta\rho^2 = 2.72 \times 10^{21}$ cm^{-4}, d_{MAO}=1.10 g/mol and the applied scaling factor $f = (6.0 \pm 1.0) \times 10^7$ we obtain for the MAO refractive index increment $(dn/dc) = 0.003 \pm 0.001$. This very low value confirms our postulated near iso-refractivity of PMAO−IP and d_8-toluene. This explains the difficulties in performing static and dynamic light scattering experiments; see also the discussion below. The large scatter in the SLS data also accounts for the low contrast due to the near iso-refractivity of PMAO−IP and d_8-toluene. In addition, one has to keep in mind that the scaling factor f has large error bars, due to the strong scatter of the SLS data. Therefore, the molecular weight of PMAO−IP given in the following is derived from the SANS data alone, for which the contrast factor $k_{SANS} = \Delta\rho^2/N_a$, see eq 1, is precisely known.

In general we found two power laws separated by an intermediate plateau in the scattering behavior of all MAO solutions, see Figure 2. This behavior divides the experimental Q range into three different regimes. (i) Most prominent is the power law $I(Q) \sim Q^{-4}$ observed in both data sets, SLS and SANS, at low Q-vectors $Q < 6 \times 10^{-3}$ Å^{-1}. Such a decay is typical of the asymptotic regime (Porod scattering), when the scattering arises from sharp interfaces between dispersed particles and solvent.[16] (ii) At intermediate Q-vectors, i.e., $6 \times 10^{-3} < Q < 10^{-1}$ Å^{-1}, a plateau is visible, which indicates a clear separation of length scales. Such a plateau is usually found if $QR_g \approx 1$, with R_g being the radius of gyration of the scattering particle (Zimm or Guinier regime).[20] (iii) Finally, at high Q-vectors, $Q > 10^{-1}$, a second power law $I(Q) \sim Q^{-2}$ evolves. That resembles the typical scattering law found for polymer chains under Θ conditions,[17] the Gaussian chain.[25]

This general scenario can be interpreted by the presence of two different species of scattering particles with strongly different radii of gyration. The larger particles are much too large such that their size cannot be precisely determined and only their asymptotic regime i is seen in our scattering experiments. For the smaller particles, on the other hand, we can precisely determine their radius of gyration from regime ii. The asymptotic regime iii of the smaller particles shows that their internal structure resembles those of linear Gaussian chains.

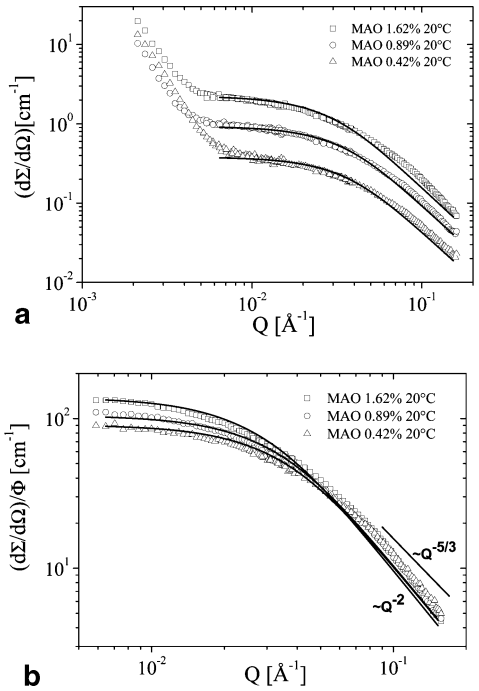

Figure 3. (a) SANS intensity in absolute units vs scattering vector Q for different volume fractions of PMAO−IP in *d*-toluene. Solid lines: Fit to the Debye form factor; see text. (b) SANS intensity normalized to volume fraction ϕ vs scattering vector Q for different volume fractions of PMAO−IP in *d*-toluene. Solid lines: Fit to the Debye form factor; see text.

This generic scattering behavior was qualitatively found for all PMAO−IP solutions. But whereas the intermediate and high Q-behavior can be reproduced quantitatively in terms of volume fraction, temperature, and applied contrast and is essentially independent from sample preparation protocol/history, the low Q-behavior, i.e., the Porod law $\sim Q^{-4}$, depends crucially on sample history and shows in addition pronounced time dependence if special precautions are not taken. Only if PMAO−IP solutions are centrifuged for an extended time (18 h at 4500 rpm) can the low-Q Porod scattering be minimized with respect to intensity and Q range. It is, though, never completely suppressed.

Figure 3a shows the concentration dependence of SANS intensities in the dilute regime with $\phi \leq 2\%$. Theses samples were centrifuged for 2 h. Whereas in the intermediate and high Q-regimes the scattering intensity systematically increases with increasing volume fraction while in the low-Q regime the intensity level, slope and onset of the Porod-like power law changes in a nonsystematic manner. Therefore, a quantitative analysis, as presented in the following sections, can only be applied to Q-vectors $Q > 10^{-2}$ Å^{-1}, as can be seen in Figure 3b, where the same data (now normalized to volume fraction ϕ) are shown. Using this representation the volume fraction dependence of eq 1 should be eliminated, as observed for high Q-vectors. Here, all data coalesce in this Q-range since SANS exclusively observes the local structure on the length scale of several tenths of an angstrom. This proves, without ambiguity, that almost all of the PMAO−IP material is present in the polymer chain structure.

Toward the low Q-vectors the curves split into a volume fraction dependent Zimm- or Guinier plateau, indicating the onset of particle−particle interactions.[20] The simplest approach to describe interactions in dilute solution is a standard virial expansion, i.e.: $\phi/I(Q=0) = 1/V_w + 2A_2\phi + ...$, which, when combined with the Guinier law $P(Q) \sim \exp(-Q^2R_g^2/3)$ for

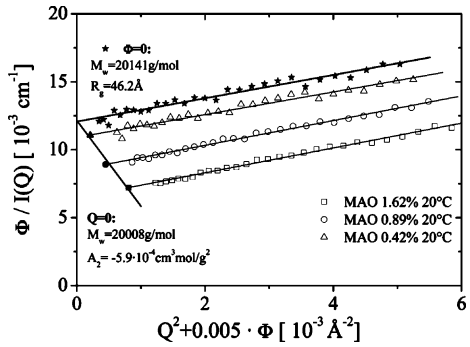

Figure 4. Zimm plot of the data shown in Figure 3. Filled stars: extrapolation to $\phi = 0$. Filled black symbols: extrapolation to $Q = 0$.

describing the Q dependence of the particle form factor $P(Q)$, results in the well-known Zimm plot.[20,26] A Zimm analysis is performed essentially without any assumption about the detailed molecular structure of the scattering particle (model-independent analysis) and reflects only its overall or global properties, i.e., the molecular volume, V_w, the radius of gyration, R_g, and, if applicable, the second virial coefficient A_2 (Using the dimensionless volume fraction ϕ as commonly applied for SANS data, $A_{2,SANS}$ has the units [mol/cm^3] if $I(Q)$ is given in units of [cm^3/mol]. The light scattering community rather uses the weight/volume concentration [g/cm^3] and therefore A_2 has the standard units [cm^3 mol g^{-2}]. Both can be easily converted by the relation: $A_{2,SANS}/d^2 = A_2$ with d, the density in [g/cm^3]). The Zimm plot of our data ($Q > 10^{-2}$ Å^{-1}) is shown in Figure 4. The dual extrapolations to zero concentration ($\phi = 0$, filled squares) and angle ($Q = 0$, filled symbols) lead to the following characteristics[27] associated with the PMAO−IP structure: $M_w = 20$ kg/mol; $D_P = \sim 311$; $A_2 = -5.9 \times 10^{-4}$ cm^3 mol/g^2; $\langle R_g \rangle_z = 46.2$ Å; $\langle R^2 \rangle_z / M = 0.637$ Å^2 mol/g while $C_\infty = 4.3$. The conversion of the measured z-average molecular weight to the weight is given elsewhere.[28]

For a detailed analysis in terms of the microscopic intramolecular structure of the scattering particles, we have to fit our SANS data to different (model) form factors to check if those can describe the experimental data over the full Q range. For "classic", polymer-like MAO, [−Al(CH$_3$)O−], in a bad to marginal solvent, the most probable form factor would be those of a Gaussian chain[17] (Debye function), $P(Q) = 2(\exp(-Q^2R_g^2) + Q^2R_g^2 - 1)/Q^4R_g^4$. The corresponding Debye curves obtained from fitting our SANS data are also shown in Figure 3a as solid lines. We fitted the different volume fractions separately, but fixed M_w and A_2 to the values obtained from the Zimm analysis where only R_g was allowed to vary as the free parameter. Certainly the Q dependence of our SANS data cannot be described over the full Q range using the Debye function. These deviations become even more pronounced if we present the SANS data in a so-called Kratky representation,[20] i.e., plotting $I(Q) \cdot Q^2$ vs Q, as shown in Figure 5. A Kratky representation reveals the existence of branched polymer structures by a peak whose height crucially depends on the degree of branching. The form factor of a linear Gaussian chain (Debye function), on the other hand, increases monotonically due to the power law $I(Q) \sim Q^{-2}$. Such a plateau is found in our experimental data only for the lowest volume fraction $\phi = 0.42\%$, but the plateau height deviates from those of the Debye function. With increasing volume fraction a slight peak evolves, which becomes clear for the highest volume fractions $\phi = 2.63\%$ and 4.30% indicating the existence of branched structures.

We have to point out that, in Figure 5, we are showing two different data sets: different with respect to sample preparation

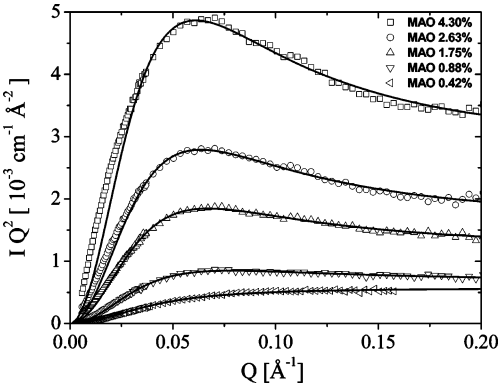

Figure 5. Kratky plot of PMAO−IP in *d*-toluene. Solid line: Fit to the polydisperse star form factor, eq 6, around the peak region.

and different with respect to the SANS setup. Whereas the high concentration data shown in Figure 1 and Figure 5 were obtained from untreated MAO solutions with a high-resolution SANS setup (*D*1.25/*C*14, *D*4/*C*14, *D*8/*C*14, *D*20/*C*20 with D = sample-to-detector distance and C = collimation length, both in meters), the low concentration data shown in Figure 3 and Figure 4 were obtained from purified (filtered/centrifuged) MAO solutions with a standard SANS setup (*D*2/*C*4, *D*8*C*8, *D*20/*C*20). Figure 5 contains data from both sets, i.e., unpurified/high-resolution SANS, 4.30%, 2.63%, 1.75%, and 0.88%, and purified/standard SANS, 0.42%. The peak in the Kratky representation is most obvious in the unpurified/high-resolution SANS data set due to the better Q resolution (trivial) and due to the higher concentration, which seems to enhance interchain branching. This now raises the crucial questions, whether M_w and R_g are varying with concentration. Actually we cannot derive a clear answer from our data for the moment without any further analysis. However, we can consider two limiting scenarios: (a) fixed, concentration independent M_w and R_g, but a strong negative second virial coefficient, which is responsible for the larger "apparent" M_w and R_g with increasing concentration; (b) a "real" variation of M_w and R_g with increasing concentration due to aggregation of individual linear PMAO−IP chains. Probably our system is in between. Any aggregation between individual particles can only occur if there exist attractive interactions. However, as noted, attractive interactions would immediately manifest themselves as a negative second virial coefficient. Thus, it is difficult to distinguish. An aggregation of linear PMAO−IP chains leading to some branched structures would also explain the occurrence of a peak in the Kratky representation, Figure 5, with increasing concentration.

Considering the synthesis of PMAO−IP, which is formed by a step growth reaction,[29] randomly branched structures might be expected. If all three methyl groups of a trimethylaluminium monomer are replaced by oxygen atoms, this monomer can form a trivalent branching point. But in this case covalent Al−O−Al bonds are formed, which should not be broken simply by dilution. Alternatively, the branching points could be created via coordinative bonds between linear MAO chains as shown in Figure 6. Here the aluminum atom switches to the coordination number of 4, instead of 3 as in the linear chain. Such a coordinative bond can depend on concentration, since the free energy of the system contains enthalpic and entropic contributions. With decreasing concentration the increase of translational and conformational entropy favors the formation of the individual linear chains.

However, the form factor for randomly branched *f*-functional polycondensates given by Burchard[30] shows no peak in the Kratky representation and is therefore not applicable. Other

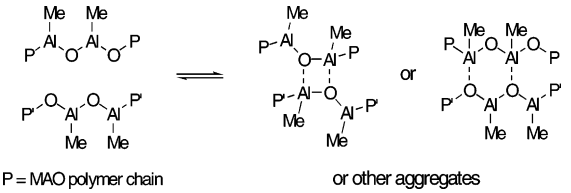

Figure 6. Linear and possible branched structures for the methylaluminoxane chain.

suitable form factors for possible nonrandomly branched polymeric structures are for example the polydisperse star form factor with a mean functionality f introduced by Burchard:[30]

$$P(Q) = \frac{1 + Q^2 R_g{}^2/3f}{(1 + Q^2 R_g{}^2 (f+1)/6f)^2} \tag{7}$$

This form factor, eq 3, is equivalent to those of a nonrandomly branched polycondensate of the ABC-type monomers, where group A can react with group B with probability β (propagation probability), or group A can react with group C with probability γ (branching probability), all other reactions are excluded.[30] In this case the mean functionality f in eq 6 is replaced by

$$f^{-1} = (\beta^2 + \gamma^2) \times \left[(\beta + \gamma) + \frac{2\beta\gamma}{1 - \beta - \gamma}\right]^{-1} \tag{8}$$

The Benoit form factor[31] for a regular Gaussian star with monodisperse arms

$$P_{star}(Q) = \frac{2}{fQ^4 R_{g,arm}{}^4} \times \left[Q^2 R_{g,arm}{}^2 - (1 - e^{-Q^2 R_{g,arm}{}^2}) + \frac{f-1}{2}(1 - e^{-Q^2 R_{g,arm}{}^2})^2\right] \tag{9}$$

also gives a peak in the Kratky representation, but is very unlikely considering the synthesis protocol of PMAO−IP.

In analyzing our SANS data we found that none of the form factors given above can describe the data over the full experimental Q range. Either we could describe the intermediate Q range around $Q \approx 10^{-2}$ Å^{-1}, i.e. the Guinier or Zimm regime, or the peak region $Q \geq 5 \times 10^{-2}$ Å^{-1} in the Kratky representation. Whereas the former results corroborate the model-independent Zimm analysis for dilute solutions $\phi \leq 2\%$, the latter gives a volume fraction dependent mean functionality f, which ranges from $f \approx 10$ at $\phi \leq 4.3\%$ to $f \approx 6$ at $\phi = 0.88\%$. The corresponding fit curves using eq 6, that describes the data best, are also shown in Figure 5. Translating f into a branching probability (eq 7) we found that only a very small degree of branching, $\beta \leq 1\%$, is needed to describe our data. Certainly there exist some other models that also give a peak in the Kratky plot, e.g., the so-called soft sphere model for hyperbranched structures.[32] So we do not claim that the polydisperse star form factor (eq 6) we used for our analysis data is the one and only correct form factor for MAO, but at least it is one reasonable interpretation of our SANS data. All other models describe far too regular structures, if one considers the synthesis protocol of MAO. The main point is, that peak in the Kratky plot clearly indicates that we observe some increasing branching with increasing concentration. The structure of the PMAO−IP branch site could involve aluminum atoms linked to either two oxygen atoms (a four membered ring) or three oxygen atoms (a six membered ring). Examples of these potential branch site architectures are given in Figure 6. The generic SANS scattering data combine to support the notion that PMAO−IP is a polymer

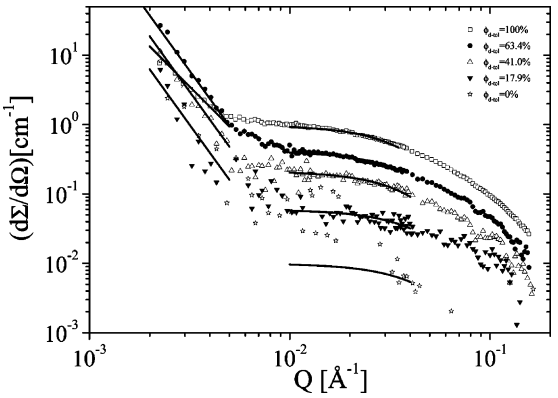

Figure 7. PMAO−IP in different d_8-toluene/h_8-toluene mixture. Solid line: Fit to Guinier function.

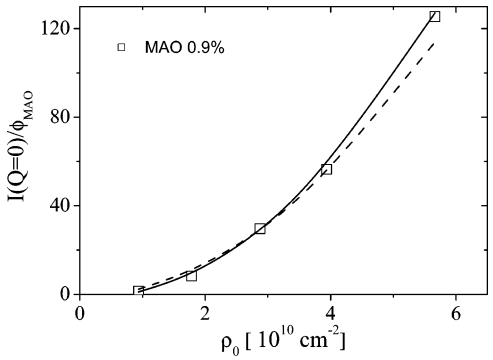

Figure 8. Zimm plateau intensity vs scattering length density of the solvent ρ_0 for PMAO−IP in different *d*-toluene/*h*-toluene mixture. Solid line: Fit M_w. Dashed line: fitting ρ_{MAO}; see text.

chain with a molecular weight (or chain length) well above those exhibited for the structures that have been based upon various theoretical exercises.[10,13−15]

If we have a concentration dependent molecular weight due to interchain branching, we also have to reconsider the results of our Zimm analysis given in the previous paragraph. In a zero order approximation we can assume that A_2 is independent of molecular weight and branching, which is reasonable for the low degree of branching observed in our experiments. So we can modify the virial expansion in the following way:

$$\phi/I(Q=0) = 1/V_w(\phi) + 2A_2\phi + ... = 1/f(\phi)V_w(\phi=0) + 2A_2\phi + ... \quad (10)$$

Here we have taken the linear chain with $M_w = 20$ kg/mol found at infinite dilution as the primary building block of the branched structures observed at higher concentrations. For the concentration dependent functionality or degree of branching $f(\phi)$, we used the values obtained from fitting the peak height in the Kratky representation. Finally we derive a corrected second virial coefficient $A_2 = -1.3 \times 10^{-4}$ cm^3 mol/g^2, which is considerably lower than $A_2 = -5.9 \times 10^{-4}$ cm^3 mol/g^2 obtained from the standard Zimm analysis, but still negative, i.e., reflecting the known bad solvent quality of toluene for MAO and also in agreement with the observed Gaussian chain behavior.

Contrast Variation. In order to investigate in greater detail the origin of additional low-*Q* scattering and corroborate the composition of the underlying scattering particles we applied contrast variation techniques,[20] i.e. dissolving unpurified PMAO−IP in different isotopic mixtures of h_8- and d_8-toluene (for details, see Table 2). Most of the PMAO−IP is present as a polymer-like structure, [−Al(CH$_3$)O−], and only a small fraction of the material is insoluble in toluene and finally forms a precipitate with a chemical composition near that of Al_2O_3. In general, the contrast in a SANS experiment is given by the difference in scattering length density between solute ρ and solvent ρ_0, eq 2, and crucially depends on its chemical composition. In particular the difference between proton H ($b_H = -3.74 \times 10^{-13}$cm) and deuteron D ($b_D = 6.65 \times 10^{-13}$ cm) allows the matching of the scattering contributions from different components by application of H/D-labeling and contrast variation. Ideally we should be able to match either the polymer-like structure or the large-scale aggregates ($\rho_{Al_2O_3} = 4.1 \times 10^{10}$ cm^{-2}).

Changing the scattering length density ρ_0 of the solvent allows us, in addition, to confirm the results from the previous full contrast experiments with respect to the molecular weight of the polymer-like PMAO−IP aggregate. Figure 7 presents the SANS data for untreated MAO solutions with volume fraction $\phi = 0.8\%$ at different contrast conditions. The generic scattering behavior is the same for all contrasts. A low-*Q* Porod scattering regime separated by a more or less well-developed Zimm-plateau from the polymer-like intensity profile found at higher *Q*-vectors is seen. The Porod scattering at low *Q*-vectors varies discontinuously and still remains visible even in fully protonated toluene. The decrease is only a factor of ≈4 compared to its maximum value found in a solvent with $\phi_{d-tol} = 63.4\%$. Surprisingly this maximum is observed exactly for the solvent composition, which matches the scattering length density of amorphous aluminum oxide, $\rho_{Al_2O_3} = 4.1 \times 10^{10}$ cm^{-2}. However, we have to keep in mind the following experimental difficulties while interpreting this finding: (i) We cannot overcome the time-dependent precipitation of the material forming the large-scale aggregates, although we tried to perform all experiments approximately at the same time after sample preparation. (ii) The chemical composition of the precipitating material forming the large-scale aggregates might also show a time dependence and in addition vary slightly between the samples. Therefore, we can only conclude that the particles, which are responsible for the Porod scattering, still contain protonated material and do not consist solely of Al_2O_3.

In contrast, at intermediate and high *Q* vectors, the scattering intensity continuously decreases by approximately 2 orders of magnitude with increasing volume fraction of protonated toluene until nearly no intensity at all is left. For parametrizing the data we fitted the decay from the plateau level either by a Guinier function, $I(Q) = A \exp(-Q^2R_g^2/3)$, or by the Beaucage form factor[33] separately for each contrast. Within error bars the corresponding radius of gyration remains at a constant value of $R_g \approx 40 \pm 2$Å, only for $\phi_{d-tol} = 18.0\%$ we found a slightly smaller value of $R_g \approx 34 \pm 5$ Å. The forward scattering or amplitude is given by $A = I(Q=0) = (\rho_{MAO} - \rho_0)^2/N_a\phi V_w$; see eq 1. Therefore, if we plot A/ϕ vs ρ_0 we can derive ρ_{MAO}− while fixing all other parameters to the previously obtained results−and compare it to the expected value calculated from chemical analysis. (Or we can derive M_w while fixing ρ_{MAO}). The SANS data in terms of $I(Q=0)/\phi$ vs ρ_0 and the resulting fit curves are shown in Figure 8. We obtain values of $\rho_{MAO} = (1.4 \pm 0.8) \times 10^9$ cm^{-2} (dashed line) or $M_w = 22000 \pm 1000$ g/mol (solid line), respectively. The large error bar of ρ_{MAO} and its substantially lower value compared to the expected $\rho_{MAO} = 4.45 \times 10^9$ cm^{-2} shows the insensitivity of the fit to this parameter. Here we have to mention that if we only analyze samples with $\phi_{d-tol} \geq 41.0\%$, i.e., those data sets with highest experimental accuracy, we nearly obtain the calculated value of ρ_{MAO}. In contrary, while fitting M_w we obtain a value that

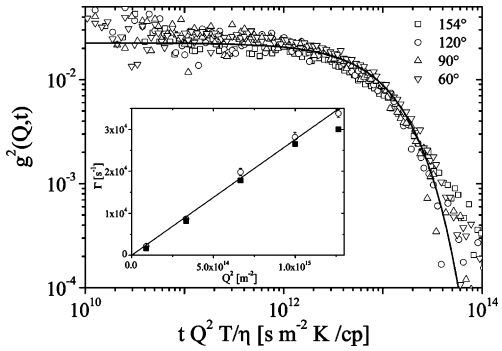

Figure 9. Intensity autocorrelation functions $g^2(Q,t)$ obtained at different scattering angles (vectors) for PMAO−IP in *d*-toluene vs the reduced time axis, solid line: single-exponential decay. Inset: Relaxation frequency vs Q^2. Closed symbols: CONTIN. Open symbols: single exponential.

differs only by approximately 10% from the results of the Zimm analysis.

PMAO—IP Phase Separation. A feature of MAO is its recognized nonsolubility in alkane solvents and the poor solubility in toluene. The negative nature of the measured A_2 fortifies this latter conclusion. Flory−Huggins theory[34] predicts that a polymer solution phase separates if the polymer−solvent interaction parameter χ becomes larger than a critical value χ_c, which can be approximated by $\chi_c \approx {}^1/_2 + D_P{}^{-1/2}$. In general χ is a function of temperature, concentration and molecular weight, i.e., $\chi(T,\phi,D_P)$ and for dilute solutions it can be calculated from the second virial coefficient A_2 by $\chi \approx {}^1/_2 - d^2V_1A_2$, with d the polymer density and V_1, the molar volume of the solvent. Analysis of the scattering data using the corrected Zimm plot, see Figure 4, gives a value of $A_2 = -1.3 \times 10^{-4}$ cm^3 mol g^{-2} for PMAO−IP in d_8-toluene. Therefore, we can calculate $\chi \approx 0.52$ using $V_1 = 100.2$ g mol^{-1}/0.964 g cm^{-3} = 105.9 cm^3 mol^{-1} for d_8-toluene and $d_{MAO} \approx 1.10$ g/cm^3 for MAO. From the same fit, we obtain a molecular weight $M_w \approx 20$ kg/mol for the PMAO−IP polymer and a degree of polymerization $D_P = 20\,000/64.3 \approx 311$ using the molecular weight 64.3 g/mol of the monomer unit $AlOC_{1.45}H_{3.89}$. Finally we can estimate the critical value of the interaction parameter: $\chi_c \approx {}^1/_2 + ({}^1/_{311})^{-1/2} \approx 0.56$. That is $\chi \approx \chi_c$ and PMAO−IP in d_8-toluene at room temperature is apparently close to phase separation. Nevertheless. we found that all solutions under investigation were stable at room-temperature even for long storage times (weeks).

DLS. As static light scattering, all DLS experiments are rather difficult to perform and yield, in general, data with low statistics due to the already mentioned isorefractivity of PMAO−IP and d_8-toluene system. This results in intensity autocorrelation functions $g^2(Q,t)$ with a very low amplitude (intercept) of approximately 10^{-2}. Nevertheless a clear decay can be observed for all scattering vectors, which in turn can be described by a slightly broadened stretched exponential, $\sim\exp(-\Gamma t)^\beta$, with a β-parameter on the order of 0.8−0.9. Figure 9 shows $g^2(Q,t)$ measured at different scattering angles Θ obtained for PMAO−IP at a volume fraction of approximately 5%, which has been allowed to sediment for several days; see below. Using the reduced time axis the diffusive dynamics are clearly revealed, which is further corroborated by plotting the mean relaxation frequency Γ vs Q^2, which follows a straight line (inset Figure 9). Using the Stokes−Einstein relation we can finally derive an apparent hydrodynamic radius $R_h = 124$ Å. Compared to the R_g value found for this volume fraction, R_g=116 Å (see Figure 9), we found a ratio $R_g/R_h \approx 1$, which is substantially larger than the expected value of 0.66 for a free-draining polymer chain.[35]

This obvious disagreement raises the questions of possible (partial) heterodyning in our DLS experiments. Since all data we obtained in a Q range where the scattering is strongly dominated by the large scale particles, the Porod regime in Figure 2, those might act as a quasi-static background ("local oscillators").

In the heterodyne limit[22] the Siegert relation $g^1(Q,t) = \sqrt{g^2(Q,t)-1}$ is no longer valid and has to be replaced by $g^1(Q,t) = g^2(Q,t) - 1$. Partial heterodyning[36] would manifest itself as a decrease of the amplitude or intercept of $g^2(Q,t)$. Indeed we found such very small amplitudes in all our DLS data; see Figure 9. However, a small contrast factor (isorefractivity) would also result in a decreased amplitude of $g^2(Q,t)$, that finally would be zero in the case of exact matching of the refractive indices of solvent and solute. As already explained above, the static light scattering data corroborated the near-isorefractivity of PMAO−IP and toluene. Another support for isorefractivity comes from direct observation of samples with $\phi \approx 5\%$, which we used to explore the phase behavior of MAO at low temperatures (not mentioned in this manuscript). After 1 week at $T = -20$ °C, we found some phase-separated "gel fraction" at the bottom of the sample vial, whose meniscus was extremely difficult to see, due to the near-isorefractivity. Only if one tilted the sample vial, could one clearly see that there was an immobile bottom phase.

On the other hand, the crucial ratio $x = I_{fluct}/I_{tot}$, which rules the amount of partial heterodyning is independent from the contrast, if both types of scattering particles have the same (dn/dc). Here I_{fluct} is the fluctuating or dynamic component of the scattered Intensity, I_{stat} the static or frozen component (the "local oscillator") and $I_{tot} = I_{fluct} + I_{stat}$ is the overall intensity. Therefore, partial heterodyning is an important issue. We did the following calculation to estimate its effects. We fitted the SLS intensity shown in Figure 2 to a power law decay, $I_{SLS} = aQ^{-b}$, to smooth the fluctuating experimental data. We then calculated for each scattering angle, at which DLS experiments have been performed, the ratio x given above. Here we used the results obtained from fitting the intermediate Q SANS data to calculate $I_{fluct.}$ Finally the real diffusion coefficient D was calculated from the "apparent" diffusion coefficient D_{app} obtained by analyzing $g^2(Q,t)$ assuming pure homodyne detection, by use of $D = (2 - x)D_{app}$.[36] The corresponding results are given in Table 3. By this estimation it becomes obvious, that for all scattering angles the DLS data are obtained in the strong heterodyning regime, provided that the scattering from the large particles is frozen within the experimental time range

Table 3. Effect of Partial Heterodyning for the DLS Data Shown in Figure 9[a]

Θ [deg]	$I_{SLS,exp}$ [cm^{-1}]	$I_{SLS,fit}$ [cm^{-1}]	I_{SANS} [cm^{-1}]	x	D_{app} [m^2/s]	D [m^2/s]
30	5.67E+03	7.08E+03	2.17E+00	3.07E−04	2.39E−11	4.78E−11
60	4.22E+02	3.96E+02	2.17E+00	5.48E−03	2.61E−11	5.21E−11
90	1.09E+02	8.67E+01	2.17E+00	2.50E−02	2.98E−11	5.89E−11
120	1.55E+01	3.57E+01	2.17E+00	6.08E−02	2.82E−11	5.47E−11
154	3.57E−01	2.13E+01	2.17E+00	1.02E−01	2.67E−11	5.07E−11

[a] See text.

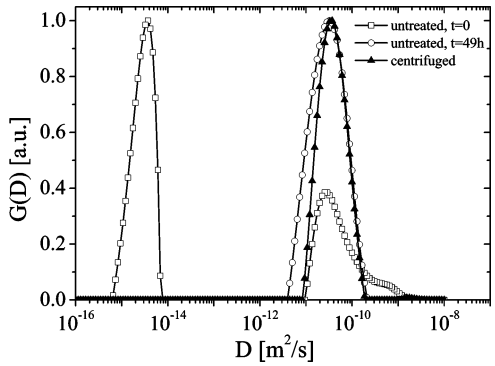

Figure 10. Intensity weighted distribution of diffusion coefficients $g(D)$ obtained by inverse Laplace transformation (CONTIN) for untreated (■,○) and centrifuged MAO solutions (▲). $\phi = 4.8\%$, $T = 20$ °C, and $\Theta = 120°$.

of DLS. The effect of partial heterodyning would also remove the discrepancy of the previously given value of ≈1 for the ratio between hydrodynamic radius R_h obtained by DLS and R_g obtained by SANS. Using the corrected diffusion coefficient we find now a value $R_h = 6.5 \pm 5$ Å, which then gives $R_h/R_g = 0.56$. This is a perfect match for the expected values of 0.57 of a polydisperse coil[35] (monodisperse coil $R_h/R_g = 0.66$).

Figure 10 shows the results of an inverse Laplace transformation (CONTIN[24]) of the DLS data as a function of sample history. Shown is the intensity weighted distribution of diffusion coefficients $g(D)$. Directly after dissolving PMAO−IP in d_8-toluene the sample shows a bimodal distribution that reflects the low-Q Porod scattering observed in the SLS/SANS experiments. After ∼2 days these large-scale aggregates have completely precipitated and only the fast mode, reminiscent of the polymer-like MAO structures, remains. Also shown are DLS data obtained from purified samples (centrifuged), which do not show the large scale aggregates peak. In addition the peak of the polymer-like MAO structures is slightly less broadened. The presence of these large aggregates (where the Q^{-4} regime was encountered) is similar to what has been seen in the *tert*-butyllithium initiation of butadiene in *n*-heptane.[37] SANS measurements showed that those large three-dimensional structures diminished in concentration as chain length increased.

PMAO—IP Chain Polydispersity. It is recognized that MAO and toluene are a near-isorefractive system (see below). This limits the use of light scattering as a quantitative structural tool. For example this effectively eliminates an accurate evaluation of the width of the polymer size distribution obtained by inverse Laplace transformation techniques (CONTIN[24]). These analysis programs are quite sensitive to baseline variations in the intensity autocorrelation function, $g^2(Q,t)$. This results in a broadening of the main peak in the distribution of relaxation times ($G(\tau)$. Therefore, we have limited the use of this DLS data to show the occurrence of a slow mode that reflects the presence of large-scale objects that are independent from the small-sized structures.

A more robust approach involves the standard cumulant analysis.[23] From the reduced second cumulant $\mu_2/\bar{\Gamma}^2$ the MAO chain polydispersity can be estimated[38] from $\mu_2/\bar{\Gamma} = \upsilon^2(M_w/(M_n - 1))$ with υ denoting the Flory exponent; $\upsilon = 0.5$. From the MAO concentration of $\phi = 4.73\%$ we obtained the mean value $\mu_2/\bar{\Gamma} = 0.26 \pm 0.04$ over the scattering angle range of 60° to 154°. This in turn leads to M_w/M_n of 2.1 ± 0.1. This value, within experimental error limits, is identical to the anticipated polydispersity (the most probable disribution)[39] of a macromolecule formed by end-linking (condensation or step growth) chemistries.

PMAO—IP Structures. The solution architecture of PMAO−IP has been found to be that of a polymer chain where the extent of branching increases as concentration increases. Figure 6 shows the structure of the potential branch sites. The model independent Zimm plot (involving the dual extrapolation to zero angle and concentration) demonstrates that the PMAO−IP in toluene at 20 °C forms a stable polymer chain. The Al−O bond strength [D^0_{298}] (Al trivalent/O divalent) is 443 kJ while that of C−C is 607 kJ/mol.[21] The MAO literature has been, for the most part, silent as to the perceived unsuitability of linear (or near linear) MAO chains.

The negative nature of the second virial coefficient displays the poor solvent character of toluene for our case where the hydrocarbon component is a mixture of the methyl and *n*-octyl groups. Normally, this negative A_2 would be expected to lead to polymer precipitation. However, precedence for the PMAO−IP polymer solution behavior exists in the literature. Poly(α-methylstyrene) shows a Θ temperature ($A_2 = 0$) of 35 °C in cyclohexane. The same is found for its counterpart, polystyrene. The precipitation temperatures though show marked differences[40−42] where the poly(α-methylstyrene), at a given molecular weight and concentration, will remain in solution while the equivalent polystyrene has precipitated. These differences narrow (at constant concentration) as chain molecular weights increase.

Conclusions

The unanticipated high polymer structure of the PMAO−IP as deduced from SANS, SLS and DLS is vastly different from the small, compact architectures favored for many years.[10,13,14] The ^{1}H NMR, elemental analysis and scattering experiments have clearly shown that most of the PMAO−IP forms polymeric structures with [−Al(CH_3)O−], as monomer unit where CH_3 is partially replaced by higher alkyl chains. Model-independent analysis in terms of a Zimm-plot gives $M_w = 20$ kg/mol, which corresponds to an average degree of polymerization $D_P \sim 311$ and a radius of gyration $R_g = 46.2$ Å. The observed negative virial coefficient $A_2 = -1.3 \times 10^{-4}$ cm^3 mol/g^2 reflects the poor solubility of PMAO−IP in toluene. With increasing volume fraction these polymeric structures become slightly branched with a branching probability $\beta \leq 1\%$, probably by interchain coordinative Al−O branch points (see Figure 6).

About 0.8% of the PMAO−IP forms large-scale aggregates with a size $R \geq 1000$ Å. Because of the higher oxygen/aluminum ratio and lower alkyl content compared to the overall material we can assume these aggregates are located compositionally and structurally between "classical" MAO, [−Al(CH_3)O−], and aluminum oxide Al_2O_3. This work has led to the finding of a new and unsuspected organometallic polymer species.

Note Added after ASAP Publication. This article was published ASAP on June 12, 2007. In the second paragraph of the Results and Discussion Section, the contrast factors for SANS and SLS have been changed. The correct version was published on June 13, 2007.

References and Notes

(1) Sinn, H.; Kaminsky, W.; Vollmer, H. J. *Angew. Chem., Int. Ed.* **1980**, *19*, 390.
(2) Sinn, H.; Kaminski, W. *Adv. Organomet. Chem.* **1980**, *18*, 99.
(3) (a) Resconi, L.; Cavallo, L.; Fait, A.; Piemontesi, F. *Chem. Rev.* **2000**, *100*, 1253. (b) Coates, G. W. *Chem. Rev.* **2000**, *100*, 1223. Deviation from single site behavior was reported herein. Evidence was given that supported the notion that there was a coexistence of two active species with differing rates of propagation and termination.

(4) Coates, G. W.; Hustad, P. D.; Reinartz, S. *Angew. Chem., Int. Ed.* **2002**, *41*, 2236.
(5) Sinn, H.; Schimmel, I.; Ott, M.; von Thienou, N.; Harder, A.; Hagendorf, W.; Heitmann, B.; Haupt, E. In *Metallorganic Catalysts for Synthesis and Polymerization*; Kaminsky, W., Ed.; Springer-Verlag: Berlin, 1999, p 105.
(6) Zukarov, I. I.; Zukarov, V. A. *Macromol. Theory Simul.* **2001**, *10*, 108.
(7) Imhoff, D. W.; Simeral, L. S.; Sangokoya, S. A.; Peel, J. H. *Organometallics* **1998**, *17*, 1941.
(8) von Lacroix, K.; Heitmann, B.; Sinn, H. *Macromol. Symp.* **1995**, *97*, 137.
(9) Bryant, P. L.; Harwell, C. R.; Mrse, A. A.; Emery, E. F.; Gan, Z.; Caldwell, T. J.; Reyes, A. P.; Kuhns, P.; Hoyt, D. W.; Simeral, L. S.; Hall, R. W.; Butler, L. G. *J. Am. Chem. Soc.* **2001**, *123*, 12,009.
(10) Pedeutour, J.-N.; Radhakrishan, K.; Cramail, H.; Deffieux, A. *Macromol. Rapid. Commun.* **2001**, *22*, 1095.
(11) Babushkin, D. E.; Britzinger, H.-H. *J. Am. Chem. Soc.* **2002**, *124*, 12,869.
(12) Hanson, E. W.; Blom, R.; Kvernberg, P. O. *Macromol. Chem. Phys.* **2001**, *202*, 2880.
(13) Zurek, E.; Ziegler, T. *Prog. Polym. Sci.* **2004**, *29*, 107.
(14) Pasynkiewicz, S. *Polyhedron* **1990**, *9*, 429.
(15) Ystenes, M.; Eilertsen, J. L.; Liu, J.; Ott, M.; Rytter, E.; StØneng, J. A. *J. Polym. Sci., Part A: Polym. Chem.* **2000**, *38*, 3106.
(16) Porod, G. *Kolloid Z.* **1951**, *124*, 83.
(17) Debye, P. *J. Chem. Phys.* **1946**, *14*, 636.
(18) The PMAO-IP sample was prepared via a nonhydrolytic method (the IP stands for "improved performance"). See Akzo Nobel technical bulletin MA 03.324.02/December 2003. Also see: Smith, G.; Palmaka, S.; Rogers, J.; Malpass, D. US 5,831,109, November 3, 1998.
(19) Morton, M.; Fetters, L. J. *Rubb. Rev.* **1975**, *48*, 359.
(20) Higgins, J.; Benoit, H. *Polymers and Neutron Scattering*; Oxford University Press: Oxford, U.K., 1994.
(21) *Handbook of Chemistry and Physics*, 60th ed.; Weast, R. C., Ed.; CRC Press: Boca Raton, FL, 1980; Section F-220.
(22) Pecora, R.; Berne, B. J. *Dynamic Light Scattering*; J. Wiley&Son, New York, 1976.
(23) Koppel, D. E. *J. Chem. Phys.* **1972**, *57*, 4814.
(24) Provencher, S. W. *Comput. Phys. Commun.* **1982**, *27*, 213, 229.
(25) Flory, P. J. *Principles of Polymer Chemistry*; Cornell University Press: Ithaca, NY, 1953; pp 402−410.
(26) Zimm, B. *J. Chem. Phys.* **1948**, *16*, 1093.
(27) M_w denotes the chain weight average molecular weight, D_p is the weight average chain degree of polymerization based upon the molecular weight of the PMAO-IP monomer unit (64.3 g/mol), and A_2 is the second virial coefficient, R_g the radius of gyration, and R^2 the root-mean-square end-to-end distance. C_∞ is the dimensionless characteristic ratio of Flory $\lfloor m_b\langle R^2\rangle_0/M_0^2\rfloor$ where m_b is the mean molecular weight per backbone bond and l_0 the Al−O bond length (1.68Å). The *z*-average molecular weight is converted to the weight average value by $\langle R_g^2\rangle_w = (U + 1)/(2U + 1)\langle R_g^2\rangle_z$ where U is dependent upon sample polydispersity $U = M_w/M_n - 1$.
(28) Kirste, R. G.; Oberthür, R. C. *Small Angle X-ray Scattering*; Glatter, O., Kratky, O., Eds. Academic Press: London. 1982.
(29) See ref. 14, pp 438 and 439 for a possible polymer synthetic scenario for MAO. The chain-end structure of poly(MAO) would be $[(CH_3)_2$-Al−O−)].
(30) Burchard, W. *Macromolecules* **1977**, *10*, 919.
(31) Benoît, H. *J. Polym. Sci.* **1953**, *11*, 507.
(32) Burchard, W.; Kajiwara, K.; Nerger, D. J. *Polym. Sci., Polym. Phys. Ed.* **1982**, *20*, 157.
(33) Beaucage, G. J. *J. Appl. Crystallogr.* **1995**, *28*, 717.
(34) Flory, P. J. *Principles of Polymer Chemistry*; Cornell University Press: Ithaca, NY, 1953; pp 502−503, 505−506, and 510−511.
(35) Burchard, W. *Adv. Polym. Sci.* **1983**, *48*, 1.
(36) Joosten, J. G. H.; McCarthy, J. L.; Pusey, P. N. *Macromolecules* **1991**, *24*, 6690.
(37) Niu, A. Z.; Stellbrink, J.; Allgaier, J.; Willner, L.; Radulescu, A.; Richter, D.; Koenig, B. W.; May, R. P.; Fetters, L. J. *J. Chem. Phys.* **2005**, *122*, 134906.
(38) Selser, J. C. *Macromolecules* **1979**, *12*, 909.
(39) Flory, P. J. *Principles of Polymer Chemistry*; Cornell University Press: Ithaca, NY, 1953; pp 318−334.
(40) Mays, J.; Hadjichristidis, N.; Lindner, J. S. *Polym. Commun.* **1989**, *30*, 174.
(41) Mays, J. W.; Hadjichristidis, N.; Wilson, W. W.; Lindner, J. S. *Macromolecules* **1991**, *24*, 6725.
(42) Li, J.; Harville, S.; Mays, J. W. *Macromolecules* **1997**, *30*, 466.

MA062940V